J. Fluid Mech. (2007), *vol.* 592, *pp.* 23–49. © 2007 Cambridge University Press
doi:10.1017/S0022112007008269 Printed in the United Kingdom

Stability of miscible core–annular flows with viscosity stratification

B. SELVAM[1], S. MERK[1], RAMA GOVINDARAJAN[2] AND E. MEIBURG[1]†

[1]Department of Mechanical Engineering, University of California, Santa Barbara, CA 93106, USA

[2]Engineering Mechanics Unit, Jawaharlal Nehru Centre for Advanced Scientific Research, Bangalore 560 064, India

(Received 25 January 2007 and in revised form 29 June 2007)

The linear stability of variable viscosity, miscible core–annular flows is investigated. Consistent with pipe flow of a single fluid, the flow is stable at any Reynolds number when the magnitude of the viscosity ratio is less than a critical value. This is in contrast to the immiscible case without interfacial tension, which is unstable at any viscosity ratio. Beyond the critical value of the viscosity ratio, the flow can be unstable even when the more viscous fluid is in the core. This is in contrast to plane channel flows with finite interface thickness, which are always stabilized relative to single fluid flow when the less viscous fluid is in contact with the wall. If the more viscous fluid occupies the core, the axisymmetric mode usually dominates over the corkscrew mode. It is demonstrated that, for a less viscous core, the corkscrew mode is inviscidly unstable, whereas the axisymmetric mode is unstable for small Reynolds numbers at high Schmidt numbers. For the parameters under consideration, the switchover occurs at an intermediate Schmidt number of about 500. The occurrence of inviscid instability for the corkscrew mode is shown to be consistent with the Rayleigh criterion for pipe flows. In some parameter ranges, the miscible flow is seen to be more unstable than its immiscible counterpart, and the physical reasons for this behaviour are discussed.

A detailed parametric study shows that increasing the interface thickness has a uniformly stabilizing effect. The flow is least stable when the interface between the two fluids is located at approximately 0.6 times the tube radius. Unlike for channel flow, there is no sudden change in the stability with radial location of the interface. The instability originates mainly in the less viscous fluid, close to the interface.

1. Introduction

Stability investigations of immiscible multi-layer flows date back to the early work of Yih (1967), whose linear stability analysis considered the plane Couette–Poiseuille case for fluid layers of different viscosities. By means of an asymptotic long-wave analysis, he was able to show that such flows can be linearly unstable to an interfacial mode for all non-zero Reynolds numbers. At the origin of this instability is the slope discontinuity of the base velocity profile at the interface, as pointed out by Smith (1990) and Charru & Hinch (2000). Hickox (1971) extended Yih's work to flows in cylindrical tubes under both axisymmetric and helical perturbations, and to fluids of different densities. Similar to the plane case, the flow was found to be unstable for any

† Author to whom correspondence should be addressed.

https://doi.org/10.1017/S0022112007008269 Published online by Cambridge University Press

non-zero Reynolds number. In contrast to the above long-wave asymptotics, Hooper & Boyd (1983) focused on short wavelength perturbations. Their work showed that, in the absence of surface tension, the unbounded immiscible Couette flow of two fluids of different viscosities is always unstable. A lucid explanation of the physical mechanism underlying this instability is provided in a short note by Hinch (1984), based on the dynamics of the perturbation vorticity field.

Following these early works, Joseph and coauthors (Joseph, Renardy & Renardy 1984; Hu & Joseph 1989; Preziosi, Chen & Joseph 1989; Hu, Lundgren & Joseph 1990) performed a number of stability investigations on immiscible core–annular flows. Motivated by the application of lubricated oil pipelines, their focus was on a more viscous core. In addition to the effects of viscosity and density stratification, they also examined weakly nonlinear dynamics, issues of pattern formation and several other aspects. Comprehensive summaries of much of their work are provided in the monograph by Joseph & Renardy (1992), and in the review by Joseph *et al.* (1997). Hu & Patankar (1995) studied the linear stability of core–annular flows with viscosity and density differences in a vertical pipe with respect to asymmetric disturbances and compared with the experimental observations of Bai, Chen & Joseph (1992). More recently, nonlinear simulations of such immiscible flows have been conducted by several authors, among them Li & Renardy (1999) and Kouris & Tsamopoulos (2001*b*, 2002*b*). While the aforementioned works focused on core–annular flows in straight pipes, flows in pipes of varying cross-section have been explored as well, motivated by the modelling of irregular rock pores in secondary oil recovery. Kouris & Tsamopoulos (2001*a*, 2002*a*) investigated both linear and nonlinear dynamics of core–annular flows in periodically constricted circular tubes, whereas Wei & Rumschitzki (2002*a*, *b*) modelled the core–annular flows in an asymptotically corrugated tube. Miscible flow instabilities, which are the focus of the present investigation, to date have received much less attention than their immiscible counterparts. Hence, one our aims is to identify similarities and differences between miscible core–annular flows and their immiscible counterparts.

Several investigations have addressed the effects of miscibility for plane flow configurations. Ranganathan & Govindarajan (2001) and Govindarajan (2004) analysed the stability of miscible fluids of different viscosities flowing through a channel in a three-layer Poiseuille configuration. They obtained a broadband instability at high Schmidt numbers and low Reynolds numbers, resembling the Yih instability. Ern, Charru & Luchini (2003) considered the stability of Couette flows in the presence of a continuous but steep viscosity variation between the two layers. They found that a stable discontinuous configuration could be destabilized by diffusion. Under the assumption of infinite diffusivity, Malik & Hooper (2005) addressed the problem of non-convergence of energy growth in a two-fluid channel flow by replacing the interface with a miscible layer of variable viscosity. The aforementioned investigations all focus on the plane geometry. Even for single fluids, we know that plane channel flows can be fundamentally different from pipe flows (Drazin & Reid 1981). Hence, one of our goals is to establish the differences between miscible core–annular flows and their plane counterparts.

Scoffoni, Lajeunesse & Homsy (2001) describe experimental observations of a miscible interface instability that occurs when a less viscous lighter fluid displaces a more viscous heavier one in a vertical capillary tube. The basic flow structure far behind the tip of the finger of displacing fluid is of core–annular form, with a nominally cylindrical interface separating the injected fluid in the core from a thin film of the displaced fluid left behind on the tube wall. Depending on the ratio of

https://doi.org/10.1017/S0022112007008269 Published online by Cambridge University Press

the fluid viscosities and the normalized flow rate, this miscible interface is seen to develop axisymmetric and/or helical perturbations that eventually result in large-scale deviations from its nominally cylindrical shape. The authors hypothesize that the observed instabilities represent the miscible equivalent of the immiscible core–annular flow instabilities driven by viscosity contrasts, as discussed above. However, their observations do not address the question as to whether the existence of a density difference is a prerequisite for the instability, or if it can also form as a result of a viscosity difference alone. The present linear stability investigation intends to investigate this hypothesis in more detail. Since the experimental observations by Scoffoni *et al.* (2001) were made at low Reynolds numbers, we will pay particular attention to potential instability modes in the limit of vanishing Reynolds numbers.

Petitjeans & Maxworthy (1996), Chen & Meiburg (1996), Kuang, Maxworthy & Petitjeans (2003) and Balasubramaniam *et al.* (2005) investigated miscible variable-viscosity displacements in capillary tubes from a different perspective. Although these authors did not focus on the potentially unstable behaviour of the core–annular flow far behind the displacement front, they recorded the front propagation velocity, and the thickness of the film left behind on the tube wall, as a function of the viscosity ratio, the Péclet number, and the orientation of the tube, as an extension to the classical work by Taylor (1960) and Cox (1962) for immiscible displacements.

The paper is organized as follows. Section 2 formulates the physical problem under consideration, states the governing equations and defines the relevant dimensionless parameters. Subsequently, § 3 performs the linearization of the governing system of equations and derives the eigenvalue problem for the linear stability analysis. Section 4 describes the numerical implementation of this eigenvalue problem, and discusses the form of the base state. Sections 5 and 6 focus on the results of the stability analysis and present a parametric study. Finally, § 7 summarizes the findings of the present work.

2. Problem formulation

Consider an axisymmetric pipe into which two miscible fluids are injected at the upstream end in a concentric fashion. At the injection location, there is a sharp change in the concentration where the two fluids meet. However, as the fluids flow downstream in a core–annular fashion, the transition zone in the concentration profile near the interface becomes more spread out, owing to the effects of diffusion. The radial location of this transition zone is determined by the volume fractions of the two injected fluids.

In the present work, we aim to study the stability of such miscible core–annular flows in a cylindrical tube of radius R. Fluid 1 forms a film of constant thickness along the wall of the tube, while fluid 2 occupies the centre of the tube (cf. figure 1). The two fluids are assumed to be of equal densities but different viscosities. The axial, radial and azimuthal coordinates are denoted by z, r and θ, respectively.

2.1. *Governing equations*

We employ the incompressible Navier–Stokes equations, along with a convection–diffusion equation for species conservation

$$\nabla \cdot \boldsymbol{v} = 0, \tag{2.1}$$

https://doi.org/10.1017/S0022112007008269 Published online by Cambridge University Press

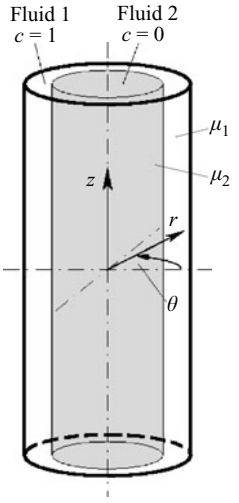


FIGURE 1. Principal sketch of a core–annular flow of two miscible fluids in a capillary tube. Fluid 1, which forms a film along the tube wall, is separated from the core fluid 2 by a diffused cylindrical interface.

$$\rho\left(\frac{\partial \boldsymbol{v}}{\partial t} + \boldsymbol{v}\cdot\nabla\boldsymbol{v}\right) = -\nabla p + \nabla\cdot\boldsymbol{\tau}, \tag{2.2}$$

$$\frac{\partial c}{\partial t} + \boldsymbol{v}\cdot\nabla c = \kappa\nabla^2 c, \tag{2.3}$$

where $\boldsymbol{v} = (v_r, v_\theta, v_z)$ denotes the flow velocity, $\boldsymbol{\tau} = \mu(\nabla\boldsymbol{v} + \nabla\boldsymbol{v}^T)$ the viscous stress tensor and c the concentration of the outer fluid. The elements of the viscous stress tensor τ_{ij} are defined in the usual way in cylindrical coordinates (Panton 1984). The diffusion coefficient κ is assumed constant throughout the mixture. This represents an approximation, and we note that earlier analyses have shown that variable diffusivity can have a significant influence on the stability of miscible interfaces (Riaz, Pankiewitz & Meiburg 2004; Vanaparthy, Barthe & Meiburg 2006). In specifying a constitutive relation between viscosity and concentration, we follow earlier works in literature (Tan & Homsy 1986; Goyal & Meiburg 2006) and assume the viscosity μ to be an exponential function of the concentration

$$\mu = \mu_2 \mathrm{e}^{Mc}, \qquad M = \ln\frac{\mu_1}{\mu_2}. \tag{2.4}$$

In order to render the above governing equations dimensionless, we choose the radius of the tube (R) as the characteristic length L^*, and the maximum viscosity (μ_1 for positive M and μ_2 for negative M) as the characteristic viscosity μ^*. The velocity averaged over the cross-section is employed as the characteristic velocity V^*

$$V^* = \frac{\dot{Q}}{\pi R^2},$$

where $\dot{Q}$ denotes the volumetric flow rate. The characteristic time and pressure are defined as

$$t^* = \frac{L^*}{V^*}, \qquad P^* = \frac{\mu^* V^*}{L^*},$$

https://doi.org/10.1017/S0022112007008269 Published online by Cambridge University Press

respectively. We thus obtain non-dimensional governing equations of the form

$$\frac{1}{r}\frac{\partial(rv_r)}{\partial r}+\frac{1}{r}\frac{\partial v_\theta}{\partial\theta}+\frac{\partial v_z}{\partial z}=0, \tag{2.5}$$

$$\begin{aligned}Re\left[\frac{\partial v_r}{\partial t}+v_r\frac{\partial v_r}{\partial r}+\frac{v_\theta}{r}\frac{\partial v_r}{\partial\theta}-\frac{v_\theta^2}{r}+v_z\frac{\partial v_r}{\partial z}\right]\\ =-\frac{\partial p}{\partial r}+\mathrm{e}^{Mc}\left[\frac{1}{r}\frac{\partial}{\partial r}\left(r\frac{\partial v_r}{\partial r}\right)+\frac{1}{r^2}\frac{\partial^2 v_r}{\partial\theta^2}+\frac{\partial^2 v_r}{\partial z^2}-\frac{v_r}{r^2}\frac{2}{r^2}\frac{\partial v_\theta}{\partial\theta}+2M\frac{\partial c}{\partial r}\frac{\partial v_r}{\partial r}\right.\\ \left.+\frac{M}{r}\frac{\partial c}{\partial\theta}\left(r\frac{\partial}{\partial r}\left(\frac{v_\theta}{r}\right)+\frac{1}{r}\frac{\partial v_r}{\partial\theta}\right)+M\frac{\partial c}{\partial z}\left(\frac{\partial v_r}{\partial z}+\frac{\partial v_z}{\partial r}\right)\right],\end{aligned} \tag{2.6}$$

$$\begin{aligned}Re\left[\frac{\partial v_\theta}{\partial t}+v_r\frac{\partial v_\theta}{\partial r}+\frac{v_\theta}{r}\frac{\partial v_\theta}{\partial\theta}+\frac{v_r v_\theta}{r}+v_z\frac{\partial v_\theta}{\partial z}\right]\\ =-\frac{1}{r}\frac{\partial p}{\partial\theta}+\mathrm{e}^{Mc}\left[\frac{1}{r}\frac{\partial}{\partial r}\left(r\frac{\partial v_\theta}{\partial r}\right)+\frac{1}{r^2}\frac{\partial^2 v_\theta}{\partial\theta^2}+\frac{\partial^2 v_\theta}{\partial z^2}-\frac{v_\theta}{r^2}+\frac{2}{r^2}\frac{\partial v_r}{\partial\theta}\right.\\ \left.+M\frac{\partial c}{\partial r}\left(r\frac{\partial}{\partial r}\left(\frac{v_\theta}{r}\right)+\frac{1}{r}\frac{\partial v_r}{\partial\theta}\right)+\frac{2M}{r}\frac{\partial c}{\partial\theta}\left(\frac{1}{r}\frac{\partial v_\theta}{\partial\theta}+\frac{v_r}{r}\right)+M\frac{\partial c}{\partial z}\left(\frac{\partial v_\theta}{\partial z}+\frac{1}{r}\frac{\partial v_z}{\partial\theta}\right)\right],\end{aligned} \tag{2.7}$$

$$\begin{aligned}Re\left[\frac{\partial v_z}{\partial t}+v_r\frac{\partial v_z}{\partial r}+\frac{v_\theta}{r}\frac{\partial v_z}{\partial\theta}+v_z\frac{\partial v_z}{\partial z}\right]=-\frac{\partial p}{\partial z}+\mathrm{e}^{Mc}\left[\frac{1}{r}\frac{\partial}{\partial r}\left(r\frac{\partial v_z}{\partial r}\right)+\frac{1}{r^2}\frac{\partial^2 v_z}{\partial\theta^2}+\frac{\partial^2 v_z}{\partial z^2}\right.\\ \left.+M\frac{\partial c}{\partial r}\left(\frac{\partial v_r}{\partial z}+\frac{\partial v_z}{\partial r}\right)+\frac{1}{r}M\frac{\partial c}{\partial\theta}\left(\frac{\partial v_\theta}{\partial z}+\frac{1}{r}\frac{\partial v_z}{\partial\theta}\right)+2M\frac{\partial c}{\partial z}\frac{\partial v_z}{\partial z}\right],\end{aligned} \tag{2.8}$$

$$Pe\left[\frac{\partial c}{\partial t}+v_r\frac{\partial c}{\partial r}+\frac{v_\theta}{r}\frac{\partial c}{\partial\theta}+v_z\frac{\partial c}{\partial z}\right]=\left[\frac{1}{r}\frac{\partial}{\partial r}\left(r\frac{\partial c}{\partial r}\right)+\frac{1}{r^2}\frac{\partial^2 c}{\partial\theta^2}+\frac{\partial^2 c}{\partial z^2}\right]. \tag{2.9}$$

This system represents the case in which fluid 1 is less viscous ($M<0$). For the case of a more viscous fluid 1 ($M>0$), the expression e^{Mc} has to be replaced by $\mathrm{e}^{M(c-1)}$. In addition to the viscosity parameter M, we obtain the Reynolds number Re and the Péclet number Pe as further dimensionless parameters

$$Re=\frac{\rho V^* R}{\mu^*},\qquad Pe=\frac{V^* R}{\kappa}.$$

They indicate the ratio of convective to diffusive transport in the momentum and species conservation equations, respectively.

3. Formulation of the stability problem

The stability problem is formulated by decomposing the variables into a z-independent quasi-steady base state and small perturbations. In the normal mode analysis, the perturbations are assumed to be periodic in the axial and azimuthal

https://doi.org/10.1017/S0022112007008269 Published online by Cambridge University Press

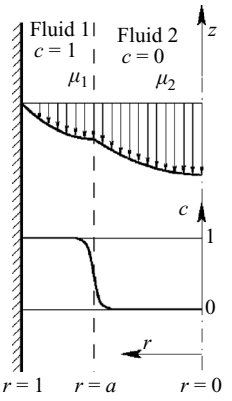


FIGURE 2. Qualitative shape of the base state velocity profile for a core–annular flow of two fluids with variable viscosity, and an initially cylindrical interface at $r = a$.

directions, with α and β denoting the respective real wavenumbers

$$\begin{pmatrix} v_r \\ v_\theta \\ v_z \\ p \\ c \end{pmatrix}(r,\theta,z,t) = \begin{pmatrix} 0 \\ 0 \\ \bar{v}_z(r) \\ \bar{p}(z) \\ \bar{c}(r) \end{pmatrix} + \begin{pmatrix} i\hat{v}_r(r) \\ \hat{v}_\theta(r) \\ \hat{v}_z(r) \\ \hat{p}(r) \\ \hat{c}(r) \end{pmatrix} \mathrm{e}^{\mathrm{i}(\alpha z+\beta\theta-\omega t)}. \tag{3.1}$$

In the usual way, this leads to an eigenvalue problem for the complex frequency $\omega = \omega_r + \mathrm{i}\omega_i$. While the imaginary part ω_i accounts for the growth of the perturbation amplitude, the real part ω_r is related to the phase velocity $c_r = \omega_r/\alpha$ of the perturbation wave.

3.1. *Base state*

We consider a downstream location where the transition zone in the concentration profile has grown diffusively to a finite thickness δ. In the following, we assume $Pe \gg 1$, so that the thickness of this mixed layer changes sufficiently slowly for the flow to be approximately parallel locally. This *a priori* assumption allows us to employ a quasi-steady parallel base state for the linear stability analysis. However, this assumption will require us to be careful when interpreting results for relatively low values of Pe, cf. below. Provided that $\delta \ll 1$, the radial concentration profile, cf. figure 2, can be approximated as

$$\bar{c}(r) = 0.5 + 0.5\mathrm{erf}\left(\frac{r-a}{\delta}\right). \tag{3.2}$$

The axial base flow must be evaluated numerically from the dimensionless axial momentum equation in the z-direction

$$\frac{\mathrm{d}\bar{p}}{\mathrm{d}z} = \mathrm{e}^{M\bar{c}}\left[\frac{\mathrm{d}^2\bar{v}_z}{\mathrm{d}r^2} + \frac{1}{r}\frac{\mathrm{d}\bar{v}_z}{\mathrm{d}r} + M\frac{\mathrm{d}\bar{v}_z}{\mathrm{d}r}\frac{\mathrm{d}\bar{c}}{\mathrm{d}r}\right]. \tag{3.3}$$

By implementing the no-slip condition $\bar{v}_z|_{r=1} = 0$ at the wall, and the symmetry condition $(\mathrm{d}\bar{v}_z/\mathrm{d}r)|_{r=0} = 0$ at the axis, the velocity profile is obtained as a function of the interface position a, the interface thickness δ, the viscosity ratio M and the pressure gradient $(\mathrm{d}\bar{p}/\mathrm{d}z)$. The pressure gradient is then adjusted so that the velocity

https://doi.org/10.1017/S0022112007008269 Published online by Cambridge University Press

averaged over the cross-section has a value of unity, as required by the above non-dimensionalization procedure.

3.2. *Perturbation equations*

Substituting (3.1) into equations (2.5)–(2.9) and linearizing around the base state provides a set of governing equations for the complex one-dimensional eigenfunctions, denoted by the $\hat{}$ symbol

$$\frac{\mathrm{d}\hat{v}_r}{\mathrm{d}r} + \frac{\hat{v}_r}{r} + \frac{\beta\hat{v}_\theta}{r} + \alpha\hat{v}_z = 0, \tag{3.4}$$

$$\begin{aligned} Re\,[-\omega\hat{v}_r + \alpha\bar{v}_z\hat{v}_r] = {} & \frac{\mathrm{d}\hat{p}}{\mathrm{d}r} - \mathrm{i}e^{M\bar{c}}\left[\frac{\mathrm{d}^2\hat{v}_r}{\mathrm{d}r^2} + \frac{1}{r}\frac{\mathrm{d}\hat{v}_r}{\mathrm{d}r} - \left(\frac{\beta^2+1}{r^2} + \alpha^2\right)\hat{v}_r\right. \\ & \left. - \frac{2\beta}{r^2}\hat{v}_\theta + 2M\frac{\mathrm{d}\bar{c}}{\mathrm{d}r}\frac{\mathrm{d}\hat{v}_r}{\mathrm{d}r} + M\alpha\frac{\mathrm{d}\bar{v}_z}{\mathrm{d}r}\hat{c}\right], \end{aligned} \tag{3.5}$$

$$\begin{aligned} Re\,[-\omega\hat{v}_\theta + \alpha\bar{v}_z\hat{v}_\theta] = {} & \frac{-\beta\hat{p}}{r} - \mathrm{i}e^{M\bar{c}}\left[\frac{\mathrm{d}^2\hat{v}_\theta}{\mathrm{d}r^2} + \frac{1}{r}\frac{\mathrm{d}\hat{v}_\theta}{\mathrm{d}r} - \left(\frac{\beta^2+1}{r^2} + \alpha^2\right)\hat{v}_\theta\right. \\ & \left. - \frac{2\beta}{r^2}\hat{v}_r + M\frac{\mathrm{d}\bar{c}}{\mathrm{d}r}\left(\frac{\mathrm{d}\hat{v}_\theta}{\mathrm{d}r} - \frac{\hat{v}_\theta}{r} - \frac{\beta\hat{v}_r}{r}\right)\right], \end{aligned} \tag{3.6}$$

$$\begin{aligned} Re\left[-\omega\hat{v}_z + \alpha\bar{v}_z\hat{v}_z + \frac{\mathrm{d}\bar{v}_z}{\mathrm{d}r}\hat{v}_r\right] = {} & -\alpha\hat{p} - \mathrm{i}e^{M\bar{c}}\left[\frac{\mathrm{d}^2\hat{v}_z}{\mathrm{d}r^2} + \frac{1}{r}\frac{\mathrm{d}\hat{v}_z}{\mathrm{d}r} - \left(\frac{\beta^2}{r^2} + \alpha^2\right)\hat{v}_z\right. \\ & + M\frac{\mathrm{d}\bar{c}}{\mathrm{d}r}\left(\frac{\mathrm{d}\hat{v}_z}{\mathrm{d}r} - \alpha\hat{v}_r\right) + M\frac{\mathrm{d}\bar{v}_z}{\mathrm{d}r}\frac{\mathrm{d}\hat{c}}{\mathrm{d}r} \\ & \left. + M\hat{c}\left(\frac{\mathrm{d}^2\bar{v}_z}{\mathrm{d}r^2} + \frac{1}{r}\frac{\mathrm{d}\bar{v}_z}{\mathrm{d}r} + M\frac{\mathrm{d}\bar{c}}{\mathrm{d}r}\frac{\mathrm{d}\bar{v}_z}{\mathrm{d}r}\right)\right], \end{aligned} \tag{3.7}$$

$$Pe\left[-\omega\hat{c} + \alpha\bar{v}_z\hat{c} + \frac{\mathrm{d}\bar{c}}{\mathrm{d}r}\hat{v}_r\right] = -\mathrm{i}\left[\frac{\mathrm{d}^2\hat{c}}{\mathrm{d}r^2} + \frac{1}{r}\frac{\mathrm{d}\hat{c}}{\mathrm{d}r} - \left(\frac{\beta^2}{r^2} + \alpha^2\right)\hat{c}\right]. \tag{3.8}$$

Our goal then is to solve for the dispersion relation

$$\omega = F\,(\alpha, \beta, Re, Pe, M, a, \delta)\,.$$

3.3. *Energy analysis*

Although the above equations determine the stability of the system, they do not provide information regarding the mechanism driving the instability. In order to gain insight into the complicated interactions between the different eigenfunction components, we carry out an analysis of the disturbance energy (Hu & Joseph 1989). The disturbance kinetic energy equation is obtained by multiplying (3.5), (3.6) and (3.7) with the complex conjugates of the perturbation velocities $\hat{v}_r^*$, $\hat{v}_\theta^*$ and $\hat{v}_z^*$, respectively. The imaginary part of the equation obtained by summing these equations and integrating over the cross-sectional area gives the required energy balance governing the growth of the perturbation

$$\dot{E} = I - D + A + B + C. \tag{3.9}$$

https://doi.org/10.1017/S0022112007008269 Published online by Cambridge University Press

Here,

$$\dot{E} = \omega_i \int_0^1 (|\hat{v}_r|^2 + |\hat{v}_\theta|^2 + |\hat{v}_z|^2)\, r\,\mathrm{d}r,$$

$$I = \int_0^1 \frac{\mathrm{d}\bar{v}_z}{\mathrm{d}r} \mathrm{Im}\{\hat{v}_r \hat{v}_z^*\}\, r\,\mathrm{d}r,$$

$$D = \frac{1}{Re} \int_0^1 \mathrm{e}^{M\bar{c}} \left[\left| \frac{\mathrm{d}\hat{v}_r}{\mathrm{d}r} \right|^2 + \left| \frac{\mathrm{d}\hat{v}_\theta}{\mathrm{d}r} \right|^2 + \left| \frac{\mathrm{d}\hat{v}_z}{\mathrm{d}r} \right|^2 + \left(\frac{\beta^2}{r^2} + \alpha^2 \right) \left(|\hat{v}_r|^2 + |\hat{v}_\theta|^2 + |\hat{v}_z|^2 \right) + \frac{1}{r^2} \left(|\hat{v}_r|^2 + |\hat{v}_\theta|^2 + 4\beta\, \mathrm{Re}\{\hat{v}_\theta \hat{v}_r^*\} \right) \right] r\,\mathrm{d}r,$$

$$A = \frac{M}{Re} \int_0^1 \mathrm{e}^{M\bar{c}} \frac{\mathrm{d}\bar{c}}{\mathrm{d}r} \frac{1}{r} \left(\frac{\mathrm{d}(r|\hat{v}_r|^2)}{\mathrm{d}r} - |\hat{v}_\theta|^2 \right) r\,\mathrm{d}r,$$

$$B = B_r + B_z = \frac{M}{Re} \left[\int_0^1 \mathrm{e}^{M\bar{c}} \frac{\mathrm{d}\bar{v}_z}{\mathrm{d}r} \mathrm{Re}\left\{ \frac{\mathrm{d}\hat{c}}{\mathrm{d}r} \hat{v}_z^* \right\} r\,\mathrm{d}r + \int_0^1 \mathrm{e}^{M\bar{c}} \frac{\mathrm{d}\bar{v}_z}{\mathrm{d}r} \mathrm{Re}\{\alpha \hat{c} \hat{v}_r^*\}\, r\,\mathrm{d}r \right],$$

$$C = \frac{M}{Re} \frac{\mathrm{d}\bar{p}}{\mathrm{d}z} \int_0^1 \mathrm{Re}\{\hat{c}\hat{v}_z^*\}\, r\,\mathrm{d}r.$$

$\dot{E}$ repesents the overall rate of change of the disturbance kinetic energy. I denotes the Reynolds stress term, which determines the rate of transfer of energy from the parallel shear flow to the disturbances, and D indicates the viscous dissipation of energy. A reflects the stress contribution due to mean viscosity gradient, while B and C quantify the stress contributions due to the viscosity perturbation, coupled to the concentration perturbation. The term B is divided into B_r (contribution due to the radial derivative of the viscosity perturbation) and B_z (contribution due to the axial derivative of the viscosity perturbation).

In the following, we indicate the associated terms in the momentum equation, in order to clarify the origin of the various above contributions: $I \Rightarrow \boldsymbol{V} \cdot \nabla \bar{\boldsymbol{V}}$, $D \Rightarrow \bar{\mu} \nabla^2 \boldsymbol{V}$, $A \Rightarrow \nabla \bar{\mu} \cdot (\nabla \boldsymbol{V} + \nabla \boldsymbol{V}^T)$, $B \Rightarrow \nabla \mu \cdot (\nabla \bar{\boldsymbol{V}} + \nabla \bar{\boldsymbol{V}}^T)$ and $C \Rightarrow \mu \nabla^2 \bar{\boldsymbol{V}}$. Note that in the above equation, $\bar{\mu} = \mathrm{e}^{M\bar{c}}$. In the C term, we have used the base state equation (3.3).

Since the magnitude of the eigenfunction is arbitrary, we normalize the eigenfunction by its maximum absolute value. In the energy analysis, it is convenient to normalize each term with respect to the total kinetic energy $\int_0^1 (|\hat{v}_r|^2 + |\hat{v}_\theta|^2 + |\hat{v}_z|^2)\, r\,\mathrm{d}r$ (Boomkamp & Miesen 1996; Govindarajan, L'vov & Procaccia 2001). For an unstable flow, $\dot{E}$ should be positive. Among the right-hand-side terms of (3.9), $-D$ is always negative, while all other terms can be positive or negative, respectively, indicating production or destruction of perturbation energy.

4. Numerical implementation of the eigenvalue problem

We employ a spectral collocation method based on Chebyshev polynomials to discretize the perturbation equations. In order to cluster the grid points in the interfacial region, we use a stretching function on the Gauss–Lobatto points (Govindarajan 2004). Upon discretization, the system of linear equations can be written in matrix form as

$$\boldsymbol{L}\hat{\phi} = \omega \boldsymbol{P} \hat{\phi}, \tag{4.1}$$

https://doi.org/10.1017/S0022112007008269 Published online by Cambridge University Press

where

$$\hat{\phi} = (\hat{v}_r, \hat{v}_\theta, \hat{v}_z, \hat{p}, \hat{c}) \ . \tag{4.2}$$

$\boldsymbol{L}$ is a 5×5 differential matrix given by

$$\boldsymbol{L} = \begin{pmatrix} L_{11} & -2\mathrm{i}e^{M\bar{c}}\beta r^{-2} & 0 & -\mathrm{D}_1 & \mathrm{i}e^{M\bar{c}}M\alpha\dfrac{\mathrm{d}\bar{v}_z}{\mathrm{d}r} \\ \mathrm{i}e^{M\bar{c}}\left(-2\beta r^{-2} - \beta M r^{-1}\dfrac{\mathrm{d}\bar{c}}{\mathrm{d}r}\right) & L_{22} & 0 & \beta r^{-1} & 0 \\ \mathrm{i}e^{M\bar{c}}\left(-\alpha M\dfrac{\mathrm{d}\bar{c}}{\mathrm{d}r}\right) + Re\,\frac{\mathrm{d}\bar{v}_z}{\mathrm{d}r} & 0 & L_{33} & \alpha & L_{35} \\ \mathrm{D}_1 + r^{-1} & \beta r^{-1} & \alpha & 0 & 0 \\ Pe\dfrac{\mathrm{d}\bar{c}}{\mathrm{d}r} & 0 & 0 & 0 & \mathrm{i}\mathrm{D}_2 + \alpha Pe\,\bar{v}_z \end{pmatrix}.$$

In the above notation, $\mathrm{D}_1 = \mathrm{d}/\mathrm{d}r$, $\mathrm{D}_2 = \mathrm{d}^2/\mathrm{d}r^2 + r^{-1}\mathrm{d}/\mathrm{d}r - (\beta^2 r^{-2} + \alpha^2)$, and

$$\begin{aligned} L_{11} &= \mathrm{i}e^{M\bar{c}}\left(\mathrm{D}_2 + 2M\frac{\mathrm{d}\bar{c}}{\mathrm{d}r}\mathrm{D}_1 - r^{-2}\right) + \alpha Re\,\bar{v}_z, \\ L_{22} &= \mathrm{i}e^{M\bar{c}}\left(\mathrm{D}_2 - r^{-2} + M\frac{\mathrm{d}\bar{c}}{\mathrm{d}r}(\mathrm{D}_1 - r^{-1})\right) + \alpha Re\,\bar{v}_z, \\ L_{33} &= \mathrm{i}e^{M\bar{c}}\left(\mathrm{D}_2 + M\frac{\mathrm{d}\bar{c}}{\mathrm{d}r}\mathrm{D}_1\right) + \alpha Re\,\bar{v}_z, \\ L_{35} &= \mathrm{i}e^{M\bar{c}}\left(M\frac{\mathrm{d}\bar{v}_z}{\mathrm{d}r}\mathrm{D}_1 + M\left(\frac{\mathrm{d}^2\bar{v}_z}{\mathrm{d}r^2} + r^{-1}\frac{\mathrm{d}\bar{v}_z}{\mathrm{d}r} + M\frac{\mathrm{d}\bar{c}}{\mathrm{d}r}\frac{\mathrm{d}\bar{v}_z}{\mathrm{d}r}\right)\right). \end{aligned}$$

$\boldsymbol{P}$ represents a 5×5 algebraic matrix with zero entries except $P_{11} = P_{22} = P_{33} = Re$ and $P_{55} = Pe$.

At the wall, we require all the velocity components and the normal derivative of the concentration to vanish. At the axis, the singular nature of the cylindrical coordinate system requires special treatment. The boundedness condition and the single-valuedness of velocity, together with the continuity equation, can be used to derive the boundary conditions at the axis (Khorrami, Malik & Ash 1989) for different azimuthal wavenumbers β as follows

$$\left.\begin{array}{lllll} \beta = 0: & \dfrac{\mathrm{d}\hat{v}_z}{\mathrm{d}r} = 0, & \hat{v}_r = 0, & \hat{v}_\theta = 0, & \dfrac{\mathrm{d}\hat{p}}{\mathrm{d}r} = 0, \quad \dfrac{\mathrm{d}\hat{c}}{\mathrm{d}r} = 0, \\ \beta = 1: & \hat{v}_z = 0, & \hat{v}_r + \hat{v}_\theta = 0, & 2\dfrac{\mathrm{d}\hat{v}_r}{\mathrm{d}r} + \dfrac{\mathrm{d}\hat{v}_\theta}{\mathrm{d}r} = 0, & \hat{p} = 0, \quad \hat{c} = 0, \\ \beta \geqslant 2: & \hat{v}_z = 0, & \hat{v}_r = 0, & \hat{v}_\theta = 0, & \hat{p} = 0, \quad \hat{c} = 0, \end{array}\right\} \tag{4.3}$$

In the non-staggered collocation method, we must specify an artificial boundary condition for the pressure at the wall. This condition is normally derived from the radial momentum equation (3.5), evaluated at the boundary, as

$$\frac{\mathrm{d}\hat{p}}{\mathrm{d}r}_{|r=1} = \mathrm{i}e^{M\bar{c}}\left[\frac{\mathrm{d}^2\hat{v}_r}{\mathrm{d}r^2} + M\alpha\frac{\mathrm{d}\bar{v}_z}{\mathrm{d}r}\hat{c}\right]_{|r=1}. \tag{4.4}$$

Khorrami (1991) shows that a non-staggered grid with the above boundary condition does not result in a loss of accuracy, as compared to a staggered grid without pressure boundary condition.

https://doi.org/10.1017/S0022112007008269 Published online by Cambridge University Press

	Pipe Poiseuille flow, $Re = 2000$					
	$\alpha = 1, \beta = 0$		$\alpha = 0.5, \beta = 1$		$\alpha = 0.25, \beta = 2$	
	c_r	c_i	c_r	c_i	c_r	c_i
SH	0.93675536	−0.06374551	0.84646970	−0.07176332	0.72551688	−0.14895301
Our code	0.93675536	−0.06374551	0.84646971	−0.07176332	0.72551688	−0.14895300

TABLE 1. Comparison of the maximum eigenvalue of the single-fluid system with corresponding data reported by SH.

The above complex generalized eigenvalue problem is solved using the software package MATLAB. The required numerical resolution depends on the interface thickness δ and is established by means of test runs. Typical calculations employ $N_r = 251$ points in the radial direction for $\delta = 0.025$. For larger δ, fewer grid points usually suffice.

4.1. *Validation*

Single-fluid Poiseuille flow in a pipe is known to be linearly stable for all Reynolds numbers. Schmid & Henningson (2001 herein refered to as SH) report numerically calculated stable eigenvalues for $Re = 2000$. Their results represent an obvious first validation case, although they do not address variable viscosity effects. The comparison of their values with present results is shown in table 1. Note that we had to rescale our data for this purpose, since we employ the average velocity as a characteristic scale, rather than the centreline velocity.

SH also provide the eigenvalue spectrum for the single-fluid system, consisting of three branches (as per the classification of Mack 1976), denoted as A (wall modes), P (centre modes) and S branches (mean speed modes). Figure 3 displays the eigenvalue spectrum obtained in the present investigation for $M = 0$, which corresponds exactly to figure 3.3 of SH. Figure 3 also indicates how the spectrum changes for $M > 0$. For the sake of clarity, we show only the leading modes of the A and P branches, along with a growing unstable mode (inside the dashed circle). As the viscosity ratio increases, the leading modes of the A and P branches do not become unstable, although the leading mode of the P branch shifts to the right as the centreline velocity increases. The new unstable mode has a phase speed close to that of the interface (note that $\bar{v}_{z|a=0.5} = 1.5$ for the single-fluid system) and may be regarded as the miscible equivalent of the interfacial mode identified by Yih (1967). A similar observation was made by Malik & Hooper (2005) for miscible plane channel flows.

As further validation, we compare representative linear stability results with direct numerical simulation data for a spatially periodic axisymmetric flow. As initial condition, the simulation employs the base state of the linear stability analysis, along with a small concentration perturbation of amplitude 10^{-4}. Figure 4 shows the comparison of the growth rate obtained from the linear analysis with corresponding simulation data. Good agreement is observed up to the time when the results begin to diverge owing to nonlinear effects. In addition, tracking the location of the maximum radial velocity with time allows us to calculate the phase velocity. The calculated value is within 1% of the linear wave speed 1.45. Good agreement is furthermore observed between the eigenfunctions obtained from the linear analysis, and corresponding nonlinear simulation data.

https://doi.org/10.1017/S0022112007008269 Published online by Cambridge University Press

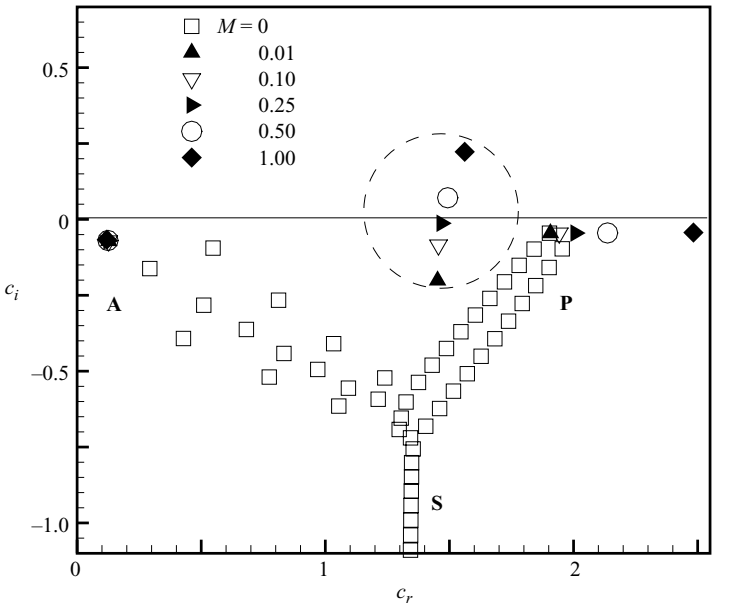


FIGURE 3. Eigenvalue spectrum for $Re = Pe = 5000$, $\alpha = \beta = 1$, $a = 0.5$ and $\delta = 0.025$. For $M = 0$, the spectrum agrees with the single-fluid results of SH. For $M > 0$, only the leading modes of the A and P branches are shown, which are stable. However, a growing mode appears (shown inside the dashed circle) whose phase velocity is close to the fluid velocity at the interface.

Additional validation information will be provided below, in the form of a comparison between miscible linear stability results and corresponding immiscible data.

5. Results

5.1. *Comparison with immiscible core–annular flow*

It is commonly assumed that a high-Péclet-number miscible flow with a thin interface will mimic the corresponding immiscible flow without interfacial tension (Scoffoni *et al.* 2001). In this section, we discuss similarities and differences, and provide quantitative comparisons for miscible and immiscible core–annular flows. For the purpose of illustration, we have developed a separate solver for the axisymmetric immiscible core–annular stability equations (Preziosi, Chen & Joseph 1989). This solver was validated by comparing with the results of Preziosi *et al.* (1989) (e.g. their figure 2) and of Hickox (1971).

In comparing our flow with an immiscible flow of two fluids separated by a sharp interface, we will discuss the effects of finite interface thickness and finite Péclet number separately. We first consider a non-zero thickness of the interface, keeping the Péclet number infinite. Figure 5(*a*) compares the dispersion relation for the axisymmetric mode of an immiscible core–annular flow ($Pe = \infty, \delta = 0$), with corresponding results for finite δ at $Pe = \infty$. The result for a very thin interface, $\delta = 0.001$, closely matches the sharp interface case. The most dangerous wavelength for the sharp interface is of the order of the tube radius, but increasing the interface thickness shifts the maximum towards longer waves. The maximum growth rate is significantly reduced. This stabilization due to increasing interface thickness is uniform

https://doi.org/10.1017/S0022112007008269 Published online by Cambridge University Press

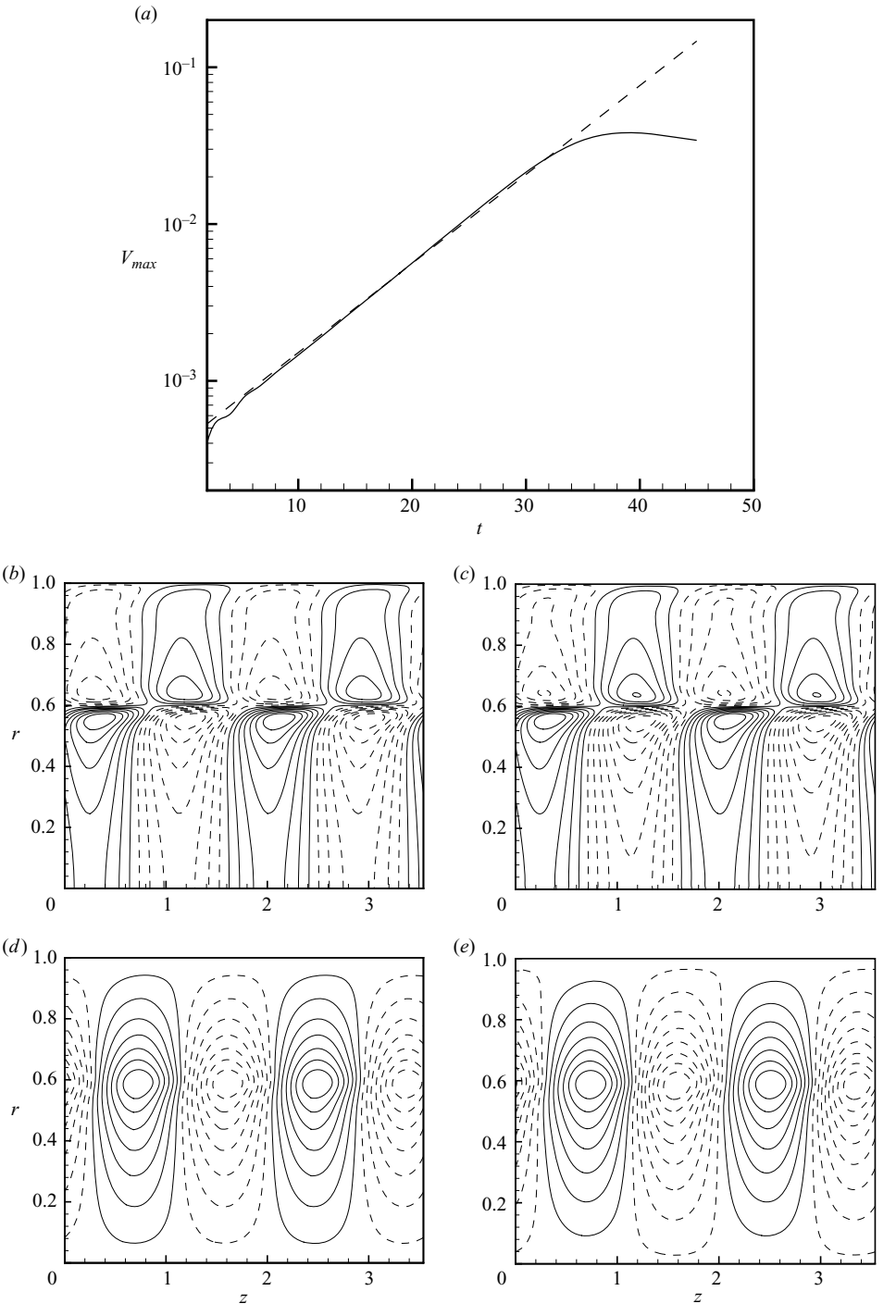


FIGURE 4. Comparison of linear stability results with nonlinear axisymmetric simulation data for $(Re, Pe, M, a, \delta) = (500, 5000, 1, 0.6, 0.02)$. (*a*) Evolution of the maximum radial velocity V_{max} with time in the nonlinear simulation (solid line), and the corresponding linear growth rate (dashed line). (*b*)–(*e*) Contour plots of the eigenfunctions and the corresponding nonlinear simulation results. (*b*) Linear analysis – $\hat{v}_z$ eigenfunction. (*c*) Nonlinear simulation – v_z perturbation. (*d*) Linear analysis – $\hat{v}_r$ eigenfunction. (*e*) Nonlinear simulation – v_r perturbation.

https://doi.org/10.1017/S0022112007008269 Published online by Cambridge University Press

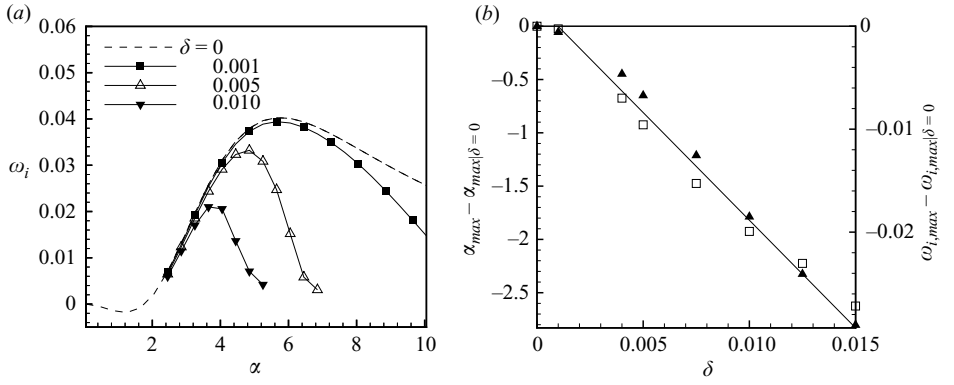


FIGURE 5. Linear stability results for $(\beta, M, Re, a) = (0, 1, 1, 0.5)$: (*a*) Dispersion relations for $Pe = \infty$ and finite interface thickness δ. The dashed line shows the sharp interface case ($Pe = \infty, \delta = 0$) without interfacial tension. Finite interface thickness stabilizes the short waves and shifts the maximum growth rate towards long waves. (*b*) The shift in the most dangerous wavenumber (□), and the reduction in the maximum growth rate (▲), as compared to the sharp interface case. Both quantities vary approximately linearly with the interface thickness.

for all flow conditions, and is discussed in detail later. Figure 5(*b*) shows the shift in the most amplified wavenumber α_{max} and the reduction of the maximum growth rate $\omega_{i,max}$ as functions of the interface thickness δ. Except for very thin interfaces, the relationship is approximately linear, indicating a scaling with δ. Note that we must exercise care in the solution procedure as the miscible equations for $Pe = \infty$ become singular at the critical point (where the phase velocity is equal to the base flow velocity) when the growth rate ω_i is zero (Ern *et al.* 2003). For this reason, we show only regions of non-zero growth rate. Incidentally, the sharp interface is stable to very long wave disturbances ($\alpha \to 0$), in agreement with Hickox's results for this parameter combination.

We now hold the interface thickness constant at $\delta = 0.005$ and discuss the effect of increasing diffusivity. Figure 6(*a*) demonstrates that lowering Pe from the ∞-limit initially increases the growth rate, which indicates that miscible core–annular flows at intermediate Pe can be more unstable than their immiscible counterparts. Beyond an intermediate Pe-value the growth rate starts to decrease, reflecting the existence of an optimal Péclet number. A similar observation had been made by Ern *et al.* (2003) for plane Couette flow. The effect of diffusivity on the most amplified wavenumber is monotonic, in that lower Pe-values shift the most dangerous mode towards long waves. Thus long waves, which are stable in the immiscible case, can become unstable when diffusion is introduced, cf. the secondary peak in figure 6(*a*). Short-wave disturbances, on the other hand, show the opposite behaviour. While the immiscible case always has a short-wave instability, as long as interfacial tension is absent (Joseph & Renardy 1992), miscible flows display a high-wave-number cut-off. These effects are also evident in the neutral stability curves in figure 6(*b*).

The non-monotonic effect of diffusivity on the stability is discussed in detail in § 6.4. At this point, we wish to point out that the dual role of diffusivity in core–annular flows is analogous to that of viscosity in parallel shear flows. There, the addition of a small amount of viscosity can destabilize an inviscidly stable flow, whereas at low Reynolds numbers, viscosity plays a stabilizing role (Panton 1984).

https://doi.org/10.1017/S0022112007008269 Published online by Cambridge University Press

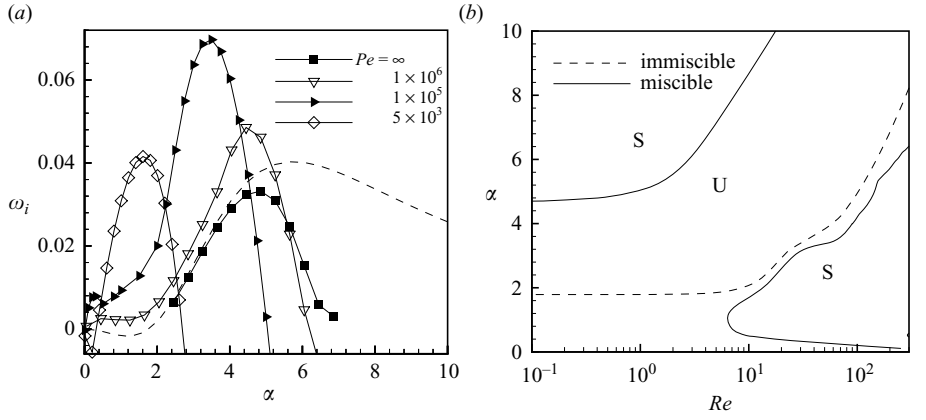


FIGURE 6. Linear stability results for $(\beta, M, a) = (0, 1, 0.5)$. (*a*) Effect of Pe on the growth rate when $\delta = 0.005$, for the parameters in figure 5. The dashed line shows the immiscible sharp interface result. Reducing Pe from ∞ initially increases the growth rate, and subsequently lowers it. Hence, the growth rate reaches a maximum at an intermediate Pe-value. (*b*) Neutral curves in the (Re, α)-plane for (i) a sharp interface without interfacial tension, where the flow is unstable above the dashed line. (ii) miscible flow with $Pe = 10^5$ and $\delta = 0.005$ (solid lines), where U and S respectively, denote the unstable and stable regions. A finite Pe destabilizes the long and stabilizes the short waves.

6. Parametric study

For analysing the influence of diffusivity, it is advantageous to distinguish between the effects of the Schmidt number $Sc = \mu^*/\rho\kappa$, and those of Pe, where $Pe = ReSc$. In the following, we take the reference parameters as $(M, Sc, a, \delta) = (\pm 1, 1, 0.5, 0.025)$, unless stated otherwise. Note that for the parameter space considered, either the axisymmetric mode ($\beta = 0$) or the corkscrew mode ($\beta = 1$) is usually found to dominate, with higher modes being less unstable or even stable. For this reason, there is no further discussion of the $\beta > 1$ modes.

6.1. *Effect of the viscosity ratio*

Figure 7 shows the neutral stability curves in the (Re, α)-plane for various positive viscosity ratios (less viscous fluid in the core). In contrast to the immiscible case, the flow is not unstable for arbitrarily small viscosity difference (Hickox 1971). For the present set of parameters, the critical viscosity ratio, below which the system is stable for all Reynolds numbers, is found to be approximately $M_{cr} = 0.11$. For viscosity ratios above M_{cr}, the flow is unstable beyond a critical Reynolds number Re_{cr}. This feature is again in contrast to the immiscible case without interfacial tension, which shows instability for all positive Reynolds numbers. Larger viscosity contrasts are more destabilizing, as they increase the slope of the base flow profile across the interface, which is the source of instability (Smith 1990). Thus, for higher viscosity contrast, the neutral curves are shifted towards lower Re. The figure indicates that the corkscrew mode is the first to destabilize, although the respective bands of unstable axial wavenumbers for the $\beta = 1$ and $\beta = 0$ modes are nearly identical. Note that for high viscosity ratios, the unstable region extends below $Re < 10$, and correspondingly Pe is less than 10. In light of our quasi-steady-state assumption, results in this parameter range have to be interpreted with caution.

It is important to know the maximum growth rate $\omega_{i,max}$, since the waves of maximum growth rate are likely to dominate the flow (Joseph & Renardy 1992).

https://doi.org/10.1017/S0022112007008269 Published online by Cambridge University Press

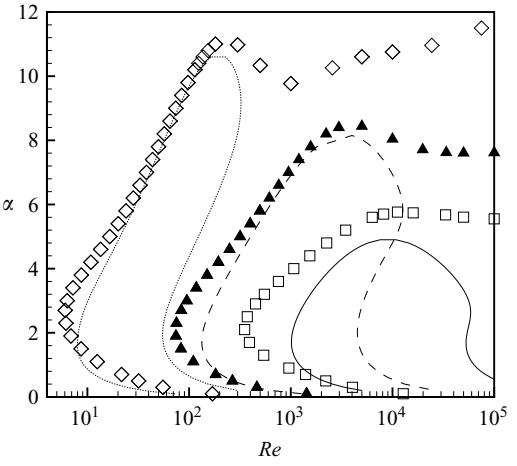


FIGURE 7. Neutral stability curves for $\beta = 1$ and $\beta = 0$, with $(Sc, a, \delta) = (1, 0.5, 0.025)$. Symbols denote the $\beta = 1$ mode for $M = 0.5$ (□), $M = 1$ (▲) and $M = 3$ (◇). Lines represent the $\beta = 0$ mode for $M = 0.5$ (solid), $M = 1$ (dashed) and $M = 3$ (dotted). Unstable regions lie inside the enclosed curves. In contrast to the immiscible case without interfacial tension, a finite viscosity contrast and a finite Reynolds number are required for an instability to develop. $\beta = 1$ destabilizes at lower Re than $\beta = 0$, although the range of unstable axial wavenumbers is comparable for both modes.

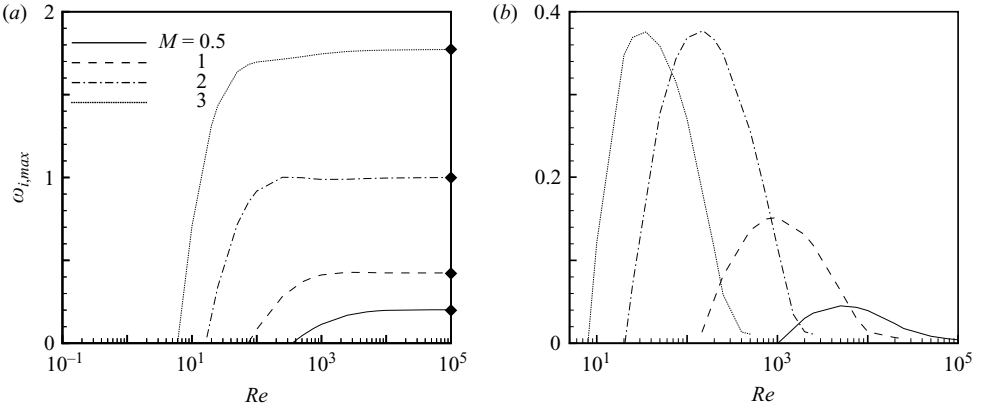


FIGURE 8. The maximum growth rate $\omega_{i,max}$ as a function of Re for positive viscosity ratios, with $(Sc, a, \delta) = (1, 0.5, 0.025)$. At high Re, the growth rate of the corkscrew mode plateaus, whereas the axisymmetric mode stabilizes. The symbol ◆ in (a) denotes the growth rate computed from the inviscid Rayleigh equation. (*a*) $\beta = 1$, (*b*) 0.

Figure 8 shows that beyond Re_{cr}, the maximum growth rate increases rapidly for both $\beta = 1$ and $\beta = 0$. However, while for $\beta = 1$ the growth rate plateaus at high Re, for $\beta = 0$ it reaches a maximum at an intermediate value of Re and then decreases again. Since the maximum growth rate of the $\beta = 1$ mode is an order of magnitude higher than for $\beta = 0$, we expect the corkscrew mode to dominate in randomly perturbed flows.

Figure 9 shows the contributions of the different terms in the perturbation energy equation for $M = 1$. The wavenumber chosen is that of the maximum growth rate at each Reynolds number. Once Re increases beyond the critical value, the net

https://doi.org/10.1017/S0022112007008269 Published online by Cambridge University Press

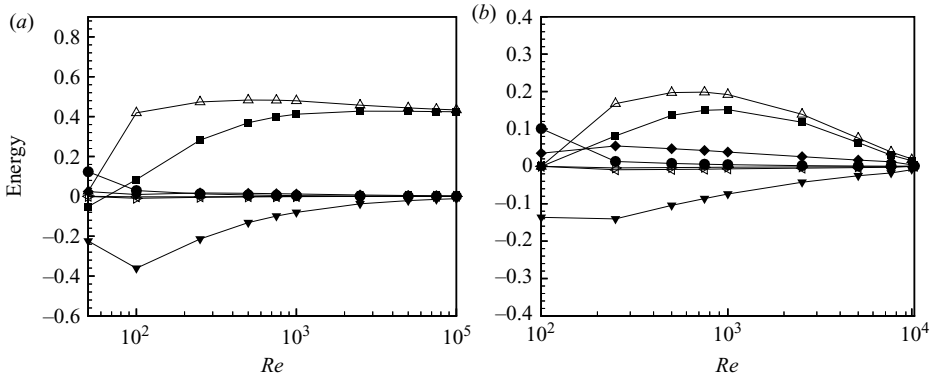


FIGURE 9. Contributions of the different terms in the perturbation energy equation for $(M, Sc, a, \delta) = (1, 1, 0.5, 0.025)$. The Reynolds stress term I represents the main source of perturbation energy production for both axisymmetric and corkscrew perturbations, exceeding the dissipation $-D$. (*a*) $\beta = 1$, (*b*) 0. ■, $\dot{E}$; △, I; ▼, $-D$; ▷, A; ◆, B_r; ◁, B_2; ●, C.

production exceeds the dissipation $-D$. Except at very low Re, where the flow is stable, the Reynolds stress term I represents the main source of energy production for both axisymmetric and corkscrew perturbations. However, we will see later that at higher Schmidt numbers, the stress terms due to the stratified viscosity play a role in destabilizing the flow. The trends seen in the growth rates are retraced in this figure, with I plateauing at large Re for $\beta = 1$, and decaying at high Re for $\beta = 0$.

The above case of $M > 0$ applies to flows in which the more viscous fluid is situated next to the wall. With respect to lubrication applications, where the thicker fluid is placed in the core, we must consider the case $M < 0$. Figure 10 shows the neutral stability curves and maximum growth rates, which indicate that for $M < 0$ the axisymmetric mode dominates. This is in contrast to the case with the thicker fluid next to the wall. While the features of the $\beta = 0$ mode are qualitatively similar for $M < 0$ and $M > 0$, the $\beta = 1$ mode now exhibits quite different properties. Both the long and the short waves are stabilized, resulting in an island of instability in the (Re, α)-plane. Moreover, the maximum growth rate decreases for larger viscosity contrasts, so that high viscosity contrasts are stable to both the axisymmetric and the corkscrew mode. Thus, for $M < 0$, the flow is most unstable at intermediate viscosity ratios.

Figure 11 shows the perturbation energy contributions for the representative case of $M = -1$. The Reynolds stress term again is the main contributor to the instability. The energy analysis thus shows that at $Sc = 1$, the physical mechanism driving the instability is the transfer of energy from the bulk flow to the perturbation via the Reynolds stresses.

Figure 12 summarizes the effect of the viscosity ratio on the critical Reynolds number Re_{cr} at low Schmidt number. The corkscrew mode and the axisymmetric mode are dominant for $M > 0$ and $M < 0$, respectively. For a given viscosity contrast, the case with the less viscous core is found to be more unstable. This is consistent with immiscible results reported by Hu & Joseph (1989) and Kouris & Tsamopoulos (2001*a*), who found the more viscous core to be relatively stable. Note that the critical Reynolds number diverges for $M = 0$, as the single-fluid system is linearly stable for all Reynolds numbers.

https://doi.org/10.1017/S0022112007008269 Published online by Cambridge University Press

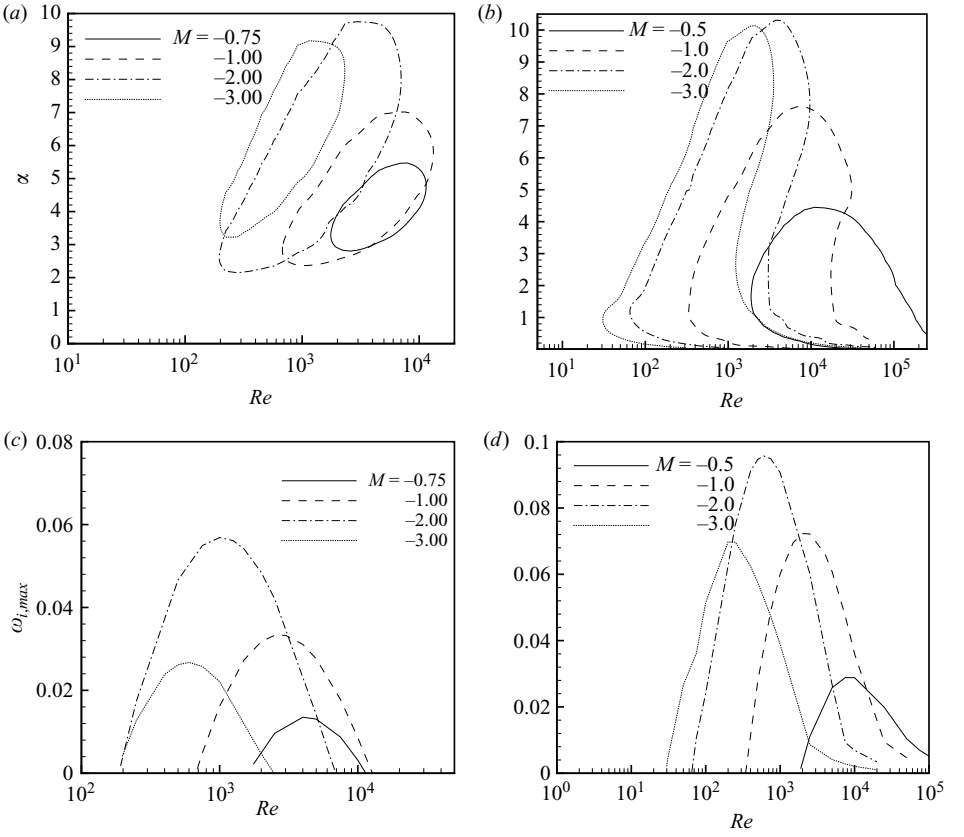


FIGURE 10. Effect of a negative viscosity ratio $M < 0$, for $(Sc, a, \delta) = (1, 0.5, 0.025)$. Unlike for the $M > 0$ case, $\beta = 0$ is now the dominant mode, and both modes stabilize at higher Re. Neutral curves: (*a*) $\beta = 1$, (*b*) 0. Maximum growth rate: (*c*) $\beta = 1$, (*d*) 0.

Referring back to figure 8, at high Re, the growth rate of $\beta = 1$ mode reaches a plateau, while that of $\beta = 0$ decreases. These trends suggest that the $\beta = 1$ mode is inviscidly unstable, while the $\beta = 0$ mode is not. In the inviscid limit ($Re \to \infty$), equations (3.4)–(3.7), after eliminating $\hat{p}, \hat{u}$ and $\hat{w}$ using continuity, yield

$$(\bar{v}_z - c)\left[\hat{v}_r'' + \frac{\hat{v}_r'}{r}\left(\frac{\alpha^2 r^2 + 3\beta^2}{\alpha^2 r^2 + \beta^2}\right) - \frac{\hat{v}_r}{r^2}\left(\frac{(\alpha^2 r^2 + \beta^2)^2 + (\alpha^2 r^2 - \beta^2)}{(\alpha^2 r^2 + \beta^2)}\right)\right] - \hat{v}_r\left[\bar{v}_z'' - \frac{\bar{v}_z'}{r}\frac{\alpha^2 r^2 - \beta^2}{\alpha^2 r^2 + \beta^2}\right] = 0. \quad (6.1)$$

Here $c = \omega/\alpha$, while a prime denotes differentiation with respect to r. Equation (6.1) represents the generalization of the inviscid Rayleigh equation for cylindrical coordinates. From this equation, the traditional Rayleigh criterion can be derived directly (Schmid & Henningson 2001). The Rayleigh criterion in cylindrical coordinates states as a necessary condition for inviscid instability that the quantity $[\bar{v}_z'' - (\bar{v}_z'/r)(\alpha^2 r^2 - \beta^2/\alpha^2 r^2 + \beta^2)]$ should change sign somewhere in the flow. Note that for $\beta = 1$, the above condition simplifies to the one given in Sahu & Govindarajan (2005), whereas for $\beta = 0$, the classical condition of $r\left(\bar{v}_z'/r\right)'$ is recovered (Drazin & Reid 1981). For positive M, this quantity never changes sign for $\beta = 0$, while it changes

https://doi.org/10.1017/S0022112007008269 Published online by Cambridge University Press

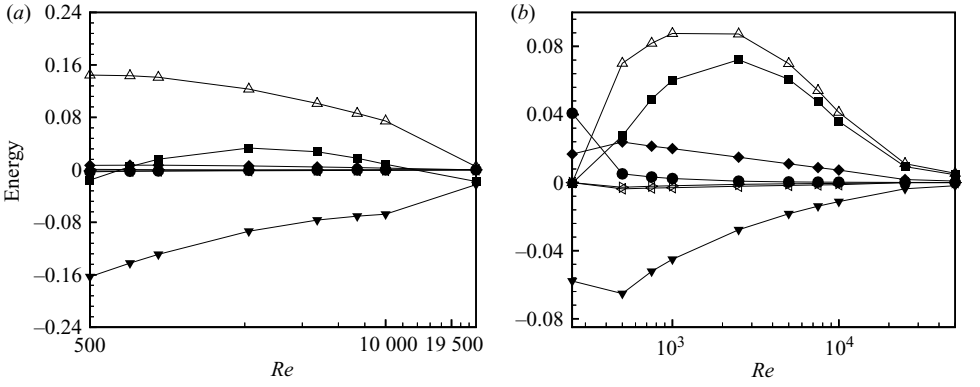


FIGURE 11. Contributions of the terms in the perturbation energy equation for $(M, Sc, a, \delta) = (-1, 1, 0.5, 0.025)$. As for $M > 0$, the Reynolds stress term I is the main contributor to the instability. (*a*) $\beta = 1$, (*b*) 0. Key as for figure 9.

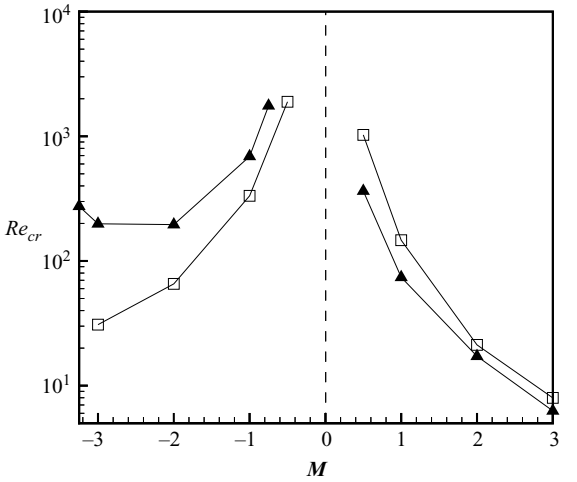


FIGURE 12. Summary of the effect of the viscosity ratio on the critical Reynolds number, when $(Sc, a, \delta) = (1, 0.5, 0.025)$. While the $\beta = 1$ mode (▲) dominates for $M > 0$, $\beta = 0$ (□) exhibits lower critical Reynolds numbers for $M < 0$.

sign only for the corkscrew mode. Moreover, in the case of negative M, neither mode satisfies the Rayleigh criterion. Thus, according to the Rayleigh criterion, only the $\beta = 1$ mode for positive M has a chance of becoming inviscidly unstable. This is consistent with our numerical results at high Re (figures 8 and 10). It should be kept in mind that the Rayleigh criterion is only a necessary, but not a sufficient condition for inviscid instability. To ascertain the inviscid instability, we solve (6.1) numerically. Note that the Rayleigh equation entails a singularity at the critical point for neutral solutions (Schmid & Henningson 2001). However, this does not pose a challenge as long as the growth rate is positive. The maximum eigenvalue computed in this way for $\beta = 1$ in the inviscid limit agrees well with the growth rate at high Reynolds number, cf. the symbol (◆) in figure 8.

https://doi.org/10.1017/S0022112007008269 Published online by Cambridge University Press

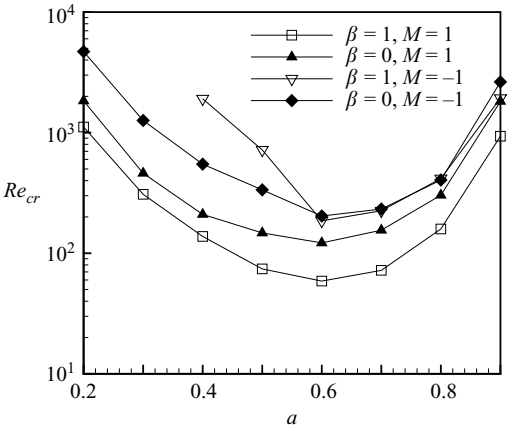


FIGURE 13. Effect of the interface location a on Re_{cr}, for $(M, Sc, \delta) = (\pm 1, 1, 0.025)$. There is an intermediate interface position near $a \approx 0.6$, for which the flow is most unstable.

6.2. *Effect of the radial location of the interface*

Figure 13 shows the critical Reynolds number for different radial interface locations a, for both the axisymmetric and the corkscrew mode, and for both positive and negative M. All the curves reach a minimum near $a = 0.6$, demonstrating that the intermediate interface location is the least stable. In the case of the more viscous fluid at the core, a narrow core completely stabilizes the $\beta = 1$ mode. In plane channel flow (Ranganathan & Govindarajan (2001); Govindarajan 2004) the flow is destabilized significantly when the mixed layer overlaps with the critical layer of the Tollmien–Schlichting (TS) mode, and thus a sudden change in Re_{cr} occurs at a particular a. In pipe flow, the TS mode does not exist (Schmid & Henningson 2001) and the dominant mode is always close to the interface. As a result, only a gradual change of Re_{cr} with a is observed. The most unstable interface location is about midway between the centreline and the wall, as discussed in the following. Consider the minimum in the neutral stability curve for the corkscrew mode at $M = 1$ and $Sc = 1$. This minimum is reached at $Re_{cr} = 59$, for $\alpha = 1.9$ and $a = 0.6$. As shown earlier, the Reynolds stress term $I = \int_0^1 I^+(r)\mathrm{d}r$ represents the main source of perturbation energy production. Figure 14(a) shows the spatial variation of the integrand $I^+(r)$ for the three different interface locations $a = 0.3$, 0.6 and 0.9. Note that the above quantities are scaled so that the dissipation $(-D)$ is unity. The Reynolds stress contribution is seen to be strongest for $a = 0.6$, resulting in the optimal perturbation amplification for this intermediate interface location. In order to understand why the Reynolds stress production is strongest for an intermediate value of a, we focus on the base flow velocity derivative $\bar{v}_z'$, which drives the Reynolds stress production. Figure 14(b) shows that this derivative is largest for the intermediate value close to $a = 0.6$. That $\bar{v}_z'$ has to have a maximum at an intermediate a-value is clear from the following argument. Both of the limits $a = 0$ and $a = 1$ correspond to single-fluid flows with a centreline velocity of 2. For intermediate a, the less viscous fluid at the core leads to a centreline velocity larger than 2, and to correspondingly larger velocity derivatives near the interface location.

The production peak is seen in figure 14(a) to be always to the left of the interface, and except when $a = 0.9$, lies close to it, which means that most of the instability is generated in the less viscous fluid. From the perspective of the less viscous fluid, the

https://doi.org/10.1017/S0022112007008269 Published online by Cambridge University Press

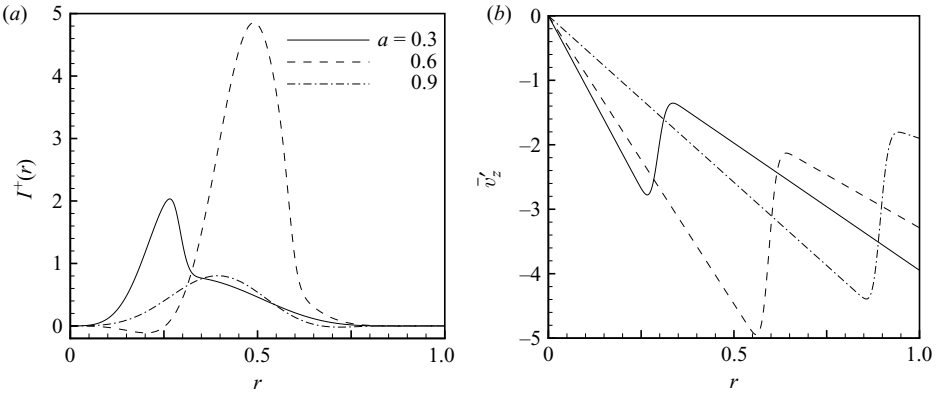


FIGURE 14. (*a*) Spatial distribution of the integrand of the Reynolds stress production term $I = \int_0^1 I^+(r)\mathrm{d}r$ for three different interface locations. The parameters correspond to the critical point for $\beta = 1$ and $M = 1$. The Reynolds stress production is strongest for $a = 0.6$, and it decreases for both narrower and wider cores. (*b*) Corresponding base flow velocity derivatives. The derivative at the interface location attains a maximum for the intermediate interface position.

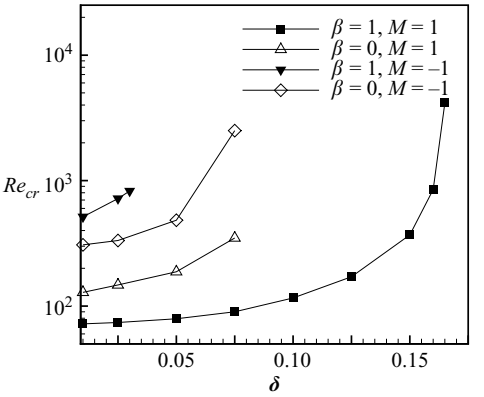


FIGURE 15. Effect of the interface thickness δ on the critical Reynolds number, for $(M, Sc, a) = (\pm 1, 1, 0.5)$. Increasing δ-values are uniformly stabilizing. In all the curves except $\beta = 1, M = 1$, the interface thickness to the right of the last data point shown is stable.

interface thus behaves in a similar way to a wall, providing shear which generates the instability. Consistently, the dissipation too shows a large increase in this region.

6.3. *Effect of interface thickness*

Figure 15 shows that thicker interfaces are uniformly stabilizing, confirming our discussion in § 5.1. Further, as seen elsewhere in the paper, for $M < 0$ and for the axisymmetric mode with $M > 0$, the regions of instability are always closed curves in the (Re, α) or (Pe, α)-planes. These regions shrink with increasing δ, and vanish at some value of δ less than 0.1. The rightmost data points presented in figure 15 for these three cases correspond to the largest δ at which instability is possible. In the case of the corkscrew mode for $M > 0$, the critical Reynolds number diverges for $\delta \sim 0.17$. Thus, we conclude that miscible core–annular flows exhibit instability only for thin interfaces, in contrast to plane Poiseuille flows, which are unstable even when

https://doi.org/10.1017/S0022112007008269 Published online by Cambridge University Press

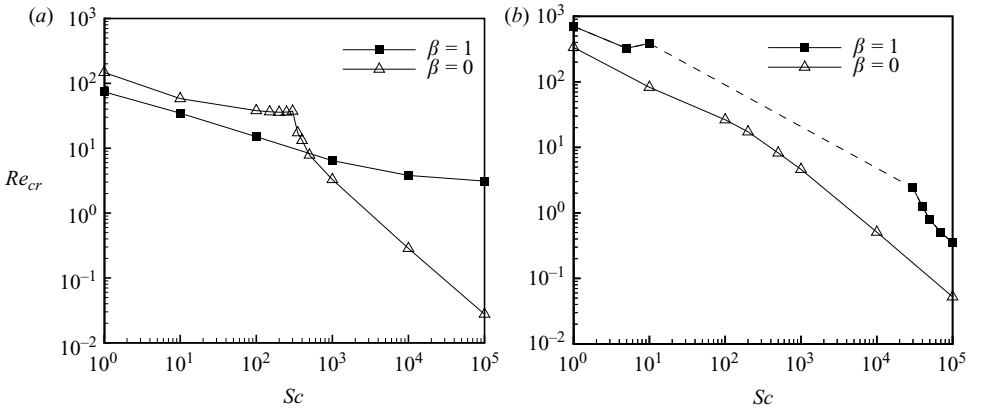


FIGURE 16. Effect of Schmidt number, when $(M, a, \delta) = (\pm 1, 0.5, 0.025)$. High Sc (reduced diffusivity) decreases the critical Reynolds number. (*a*) For $M = 1$, the axisymmetric mode overtakes the corkscrew mode at high Sc. (*b*) In the case of negative M, the destabilizing effect of Sc is not monotonic for $\beta = 1$, as there exists a window of Schmidt numbers when the flow is completely stable (shown in dashed line).

the stratification extends across the entire channel (Ranganathan & Govindarajan 2001).

6.4. *Effect of diffusivity*

Figure 16 illustrates the influence of the Schmidt number on the critical Reynolds number. For $M > 0$, increasing the Schmidt number uniformly reduces the critical Reynolds number. At low Sc, the corkscrew mode is more dangerous than the axisymmetric mode, with the opposite being true at high Sc. The crossover occurs near $Sc = 300$. For $M < 0$, the axisymmetric mode is more unstable than the corkscrew mode for all Sc (cf. figure 16*b*). In fact, there exists a window of Sc for which the corkscrew mode is stable (shown by the dashed line). In summary, at large Schmidt number, the axisymmetric mode dominates for all M.

In figure 16(*a*), we can see a break in the slope for $\beta = 0$, suggesting a change in the dominant mode. This is confirmed by the neutral stability curves in figure 17. For low Sc, the axisymmetric mode has an island of instability centreed around intermediate wave–numbers. As Sc increases, this island shrinks, until the mode becomes completely stable near $Sc = 300$. At the same time, an unstable long-wave mode appears, whose island grows as Sc is further increased. Figure 18 displays the corresponding dispersion relations for $Re = 50$. These illustrate the stabilization of the intermediate wave numbers and the destabilization of long waves as Sc increases. We observe similar behaviour for $M < 0$ and $\beta = 1$ (not shown). However, in that case the long-wave mode destabilizes at a much higher Sc, thus resulting in the window of stable Schmidt numbers seen in figure 16(*b*).

It is instructive to plot the data of figure 16(*a*) in terms of a critical Péclet number $Pe_{cr} = Re_{cr}Sc$ (figure 19). For Re less than about 3 and $M > 0$, the corkscrew mode is stable for all Péclet numbers, whereas the axisymmetric mode remains unstable above some finite Pe_{cr}. We note here that at low Re, the critical Pe is independent of Re, which suggests that the flow may be unstable in the limit $Re \to 0$. This issue will be discussed in the following section.

We now turn to the question raised in § 5.1 of why the stability at low Reynolds number depends non-monotonically on the Péclet number. Towards this end, we

https://doi.org/10.1017/S0022112007008269 Published online by Cambridge University Press

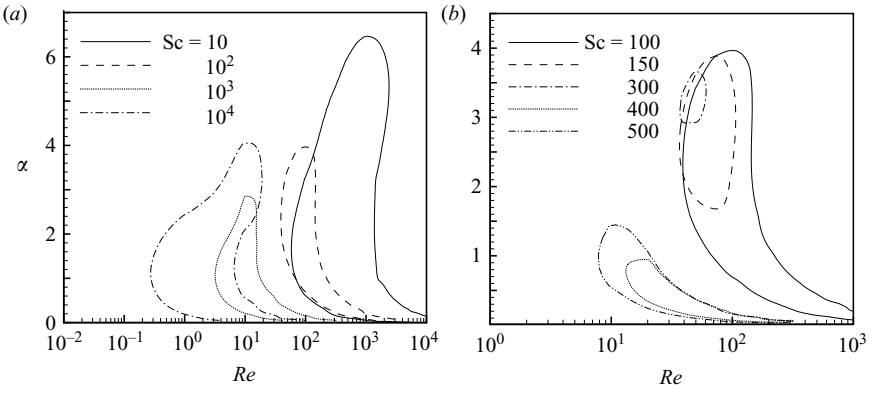


FIGURE 17. (*a*) Neutral stability curves for the $\beta = 0$ mode shown in figure 16(*a*). (*b*) Additional neutral stability curves near the crossover at $Sc = 300$. At low Sc, there is an island of instability for intermediate wavenumbers. As Sc is increased, the island shrinks and eventually disappears, while a new island appears for a long-wave mode.

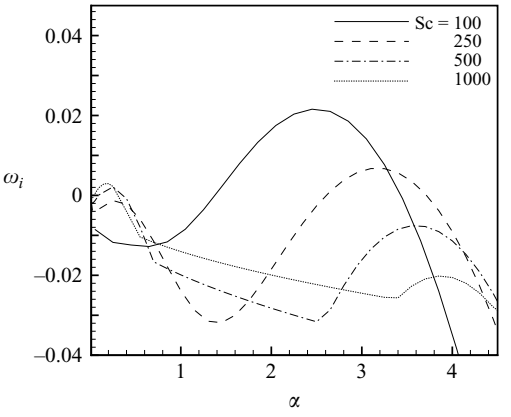


FIGURE 18. Dispersion relations for $Re = 50$, with the other parameters the same as in figure 17(*b*). As Sc increases, the intermediate wavenumbers are stabilized, and a long-wave mode goes unstable.

conduct an energy balance for the axisymmetric mode. Figure 20(*a*) illustrates how the contributions of the various terms in the perturbation energy equation change as Sc increases. For $Sc = 10$, the terms B_r and C, representing stresses arising out of viscosity stratification, whose contributions at $Sc = 1$ were quite small, are of the same order as the Reynolds stress term I. As Sc is further increased to 500 (figure 20*b*), the dominant energy balance term is altered. Now, the term B_r, which involves the radial derivative of the concentration perturbation and the base flow shear, becomes the main producer of perturbation energy. An examination of this term tells us that the integrand B_r is proportional to $\mathrm{d}\hat{c}/\mathrm{d}r$. At a given Reynolds number, increasing the Schmidt number amounts to increasing the Péclet number. As the Péclet number increases, the concentration perturbation increases in magnitude, but the region over which it is non-zero thins down in proportion to $Pe^{-1/2}$. Thus when the instability is driven by this term, a non-monotonic behaviour is displayed. The range of dominance of the axisymmetric mode corresponds to the range where this behaviour is observed.

https://doi.org/10.1017/S0022112007008269 Published online by Cambridge University Press

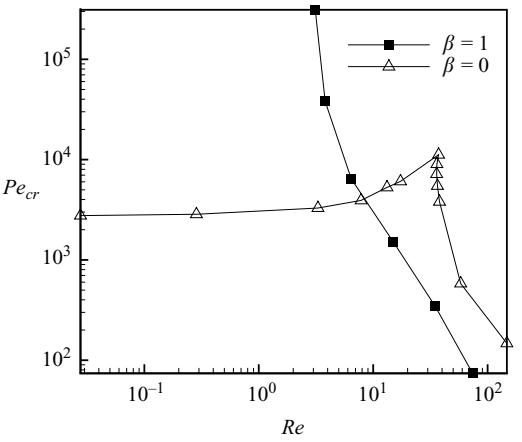


FIGURE 19. The data of figure 16(*a*) replotted in terms of a critical Péclet number Pe_{cr}. At low Reynolds number, the corkscrew mode is stable for all Péclet numbers, while the axisymmetric mode remains unstable above some finite Pe_{cr}. For $Re < O(1)$, the value of Pe_{cr} is independent of Re.

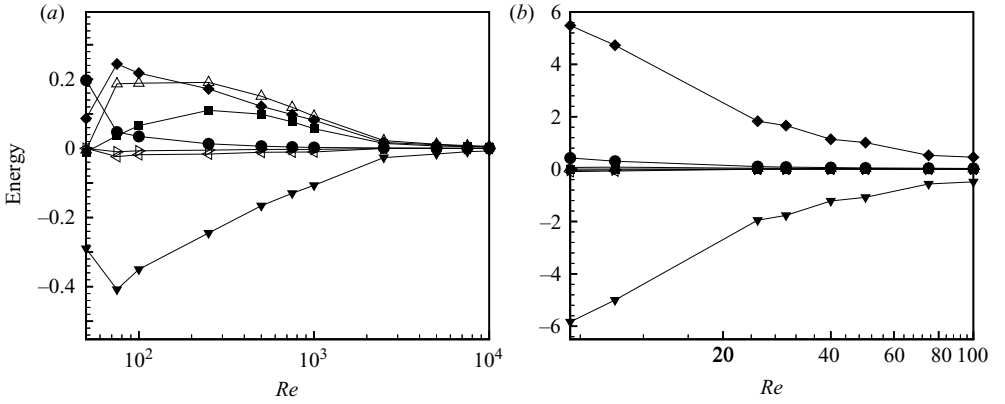


FIGURE 20. Perturbation energy balance as Sc increases, for $(\beta, M, a, \delta) = (0, 1, 0.5, 0.025)$. (*a*) $Sc = 10$, (*b*) 500. The term B_r, which involves the radial derivative of the concentration perturbation and the base flow shear, becomes the dominant perturbation energy producer. The term C also contributes to positive energy, although to a lesser extent. Key as for figure 9.

6.5. *Can miscible core–annular flow be unstable in the limit* $Re = 0$*?*

The long-wave analysis of Hickox (1971) shows that immiscible core–annular flows are linearly unstable for any non-zero Reynolds number, whereas for vanishing Reynolds number and interfacial tension, the growth rate decays to zero. Preziosi *et al.* (1989) demonstrate that immiscible core–annular flows at $Re = 0$ are unstable towards long waves whenever interfacial tension is present. In the absence of interfacial tension, however, they are neutrally stable. In contrast, the short-wave analysis of Hooper & Boyd (1983) predicts that the unbounded immiscible shear flow without interfacial tension is always unstable. However, for their results to be applicable to bounded shear flows, the disturbance wavelength should be much smaller than the radius of the tube. In light of the foregoing discussion, it will be interesting to analyse whether

https://doi.org/10.1017/S0022112007008269 Published online by Cambridge University Press

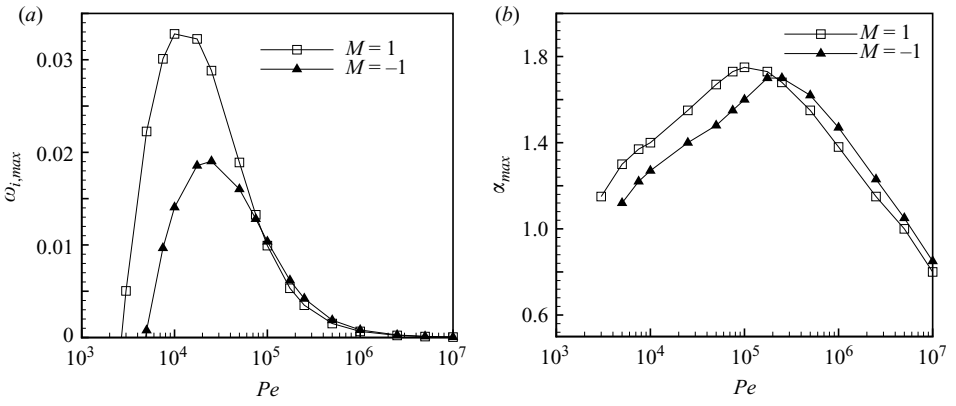


FIGURE 21. Maximum growth rate and most dangerous wavenumber as functions of Pe, for $(\beta, Re, a, \delta) = (0, 0, 0.5, 0.025)$. Miscible core–annular flows are unstable even for vanishing Reynolds number above a critical Péclet number.

miscible core–annular flows are unstable in the limit $Re = 0$, and if so, at what wavelengths. Towards this end, we employ the incompressible Stokes equations for momentum and carry out a linear stability analysis. We retain the convective terms in the concentration equation, so that we can address finite-Péclet-number flows. Note that in this limit, the Schmidt number is effectively infinite. This analysis applies to flows in which the effects of advection are negligible in the momentum equation, but not in the concentration equation.

Since the results of the previous section indicate that at low Reynolds number and large Schmidt number, $\beta = 0$ is the most unstable mode, we restrict ourselves to axisymmetric perturbations. Figure 21(a) displays the maximum growth rate as a function of Pe for $M = \pm 1$. The results show miscible core–annular flows at vanishing Reynolds number limit to be unstable, as long as Pe is sufficiently large. Note that Pe_{cr} for $M = 1$ is approximately 3×10^3, in agreement with our earlier Navier–Stokes results for low Re (cf. figure 19). For very large Pe the growth rate decreases, as the flow approaches the immiscible case.

Figure 21(b) indicates that the most dangerous wavenumbers are in the intermediate range. Hence this instability is not the miscible equivalent of the Hooper & Boyd (1983) short-wave instability. It is also not a miscible equivalent of the long-wave instability analysed by Hickox (1971) and Preziosi *et al.* (1989), since those modes require finite inertia, however small (Jiang, Helenbrook & Lin 2004). While finite diffusion and interface thickness represent important ingredients in the instability, the finite interface thickness alone cannot be at its origin, as an increasing interface thickness is stabilizing (cf. figure 22). Advection of concentration perturbations, i.e. a finite value of Pe, is a prerequisite for the instability. We wish to remark that inertialess instabilities have been encountered in two-layer flows with free surfaces, although their exact instability mechanism is not fully understood (Loewenherz & Lawrence 1989; Chen 1993; Jiang *et al.* 2004).

We note here that a core–annular type miscible-flow instability has recently been observed experimentally at Péclet number of $O(10^4$–$10^5)$ and Reynolds number less than 1 (D. Salin, personal communication).

https://doi.org/10.1017/S0022112007008269 Published online by Cambridge University Press

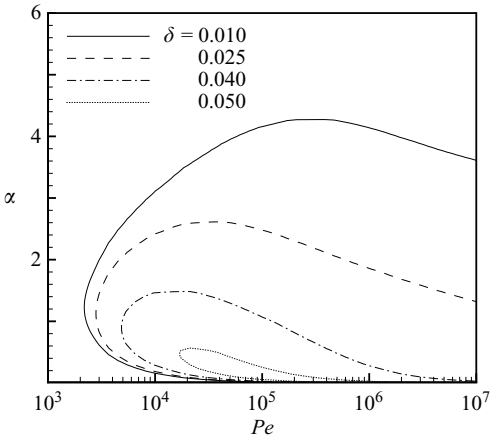


FIGURE 22. Neutral stability curves in the (Pe, α)-plane for different interface thicknesses, at $(\beta, Re, M, a) = (0, 0, 1, 0.5)$. The unstable region lies inside the curves. Increasing the interface thickness has a stabilizing influence in the limit of vanishing Reynolds number.

7. Conclusion

The current investigation addresses the temporal stability of variable viscosity, miscible core–annular flows. Such flows are distinct from their immiscible counterparts in two ways. First of all, they are characterized by a finite interface thickness, which we show to have a uniformly stabilizing effect. Hence, instabilities are seen to exist only for thin interfaces, similar to miscible two-fluid Couette flows (Ern *et al.* 2003), and in contrast to miscible plane Poiseuille flows which exhibit instability even under fully stratified conditions.

Secondly, diffusion is now present and can result in some unexpected behaviour. Specifically, we find that small amounts of diffusion (high Pe) can be destabilizing, rendering the miscible flow more unstable than a corresponding immiscible one. Low Pe, on the other hand, stabilizes the flow, consistent with the behaviour observed in plane Couette and in channel flow. Hence, there exists an optimal Péclet number at which the growth rate reaches a maximum. An energy analysis reveals that, depending on the Schmidt number, the mechanism of energy transfer from the base flow to the disturbances is either through the Reynolds stress term or via the stresses due to viscosity perturbations. The latter gives rise to the non-monotonic behaviour.

For a wide range of governing parameters, miscible core–annular flows are linearly unstable towards both intermediate and long-wave disturbances. Instability can occur even for vanishing Reynolds number. Under these conditions, the most amplified wavelength is found to be several tube diameters. This is in contrast to immiscible core–annular flows without interfacial tension, which are known to be neutrally stable towards long waves. While the axisymmetric mode is unstable at low Reynolds number, the corkscrew mode is found to be inviscidly unstable for $M > 0$. It is shown to satisfy the pipe-Rayleigh criterion above a critical viscosity ratio, consistent with the stability results for high Re.

There are many open questions regarding the nonlinear behaviour of these instabilities. In addition, the effects of density stratification and their interplay with viscosity variations hold great potential for interesting dynamics. Efforts to unravel the governing mechanisms under those conditions are currently under way.

https://doi.org/10.1017/S0022112007008269 Published online by Cambridge University Press

We thank professor G. M. Homsy for several helpful discussions. Support from the National Science Foundation under contract CTS-0456722 is gratefully acknowledged.

REFERENCES

Bai, R., Chen, K. P. & Joseph, D. D. 1992 Lubricated pipelining: stability of core–annular flow. Part 5. Experiments and comparison with theory. *J. Fluid Mech.* **240**, 97.

Balasubramaniam, R., Rashidnia, N., Maxworthy, T. & Kuang, J. 2005 Instability of miscible interfaces in a cylindrical tube. *Phys. Fluids* **17**, 052103.

Boomkamp, P. A. M. & Miesen, R. H. M. 1996 Classification of instabilities in parallel two-phase flow. *Intl J. Multiphase Flow* **22**, 67.

Charru, F. & Hinch, E. J. 2000 'Phase diagram' of interfacial instabilities in a two-layer Couette flow and mechanism for the long-wave instability. *J. Fluid Mech.* **414**, 195.

Chen, C.-Y. & Meiburg, E. 1996 Miscible displacement in capillary tubes. Part 2. Numerical simulations. *J. Fluid Mech.* **326**, 57.

Chen, K. P. 1993 Wave formation in a gravity-driven low Reynolds number flow of two liquid films down an inclined plane. *Phys. Fluids* A **5**, 3038.

Cox, B. G. 1962 On driving a viscous fluid out of a tube. *J. Fluid. Mech.* **14**, 81.

Drazin, P. G. & Reid, W. H. 1981 *Hydrodynamic Stability*. Cambridge University Press.

Ern, P., Charru, F. & Luchini, P. 2003 Stability analysis of a shear flow with strongly stratified viscosity. *J. Fluid Mech.* **496**, 295.

Govindarajan, R. 2004 Effect of miscibility on the linear instability of two-fluid channel flow. *Intl J. Multiphase Flow* **30**, 1177.

Govindarajan, R., L'vov, V. S. & Procaccia, I. 2001 Retardation of the onset of turbulence by minor viscosity contrasts. *Phys. Rev. Lett.* **87**, 174501.

Goyal, N. & Meiburg, E. 2006 Miscible displacements in Hele-Shaw cells: two-dimensional base states and their linear stability. *J. Fluid Mech.* **558**, 329.

Hickox, C. E. 1971 Instability due to viscosity and density stratification in axisymmetric pipe flow. *Phys. Fluids* **14**, 251.

Hinch, E. J. 1984 A note on the mechanism of the instability at the interface between two shearing fluids. *J. Fluid Mech.* **144**, 463.

Hooper, A. P. & Boyd, W. G. C. 1983 Shear-flow instability at the interface between two fluids. *J. Fluid Mech.* **128**, 507.

Hu, H. H. & Joseph, D. D. 1989 Lubricated pipelining: stability of core–annular flow. Part 2. *J. Fluid Mech.* **205**, 359.

Hu, H. H. & Patankar, N. 1995 Non-axisymmetric instability of core–annular flow. *J. Fluid Mech.* **290**, 213.

Hu, H. H., Lundgren, T. S. & Joseph, D. D. 1990 Stability of core–annular flow with a small viscosity ratio. *Phys. Fluids* A **2**(11), 1945.

Jiang, W. Y., Helenbrook, B. & Lin, S. P. 2004 Inertialess instability of a two-layer liquid film flow. *Phys. Fluids* **16**(3), 652.

Joseph, D. D. & Renardy, Y. Y. 1992 *Fundamentals of Two-Fluid Dynamics. Part II: Lubricated Transport, Drops and Miscible Liquids*. Springer.

Joseph, D. D., Renardy, Y. & Renardy, M. 1984 Instability of the flow of immiscible liquids with different viscosities in a pipe. *J. Fluid Mech.* **141**, 319.

Joseph, D. D., Bai, R., Chen, K. P. & Renardy, Y. Y. 1997 Core–annular flows. *Annu. Rev. Fluid Mech.* **29**, 65.

Khorrami, M. R. 1991 A Chebyshev spectral collocation method using a staggered grid for the stability of cylindrical flows. *Intl J. Numer. Meth. Fluids* **12**, 825.

Khorrami, M. R., Malik, M. R. & Ash, R. L. 1989 Application of spectral collocation techniques to the stability of swirling flows. *J. Comput. Phys.* **81**, 206.

Kouris, C. & Tsamopoulos, J. 2001*a* Core–annular flow in a periodically constricted circular tube. Part 1. Steady-state linear stability and energy analysis. *J. Fluid Mech.* **432**, 31.

Kouris, C. & Tsamopoulos, J. 2001*b* Dynamics of axisymmetric core–annular flow in a straight tube. i. The more viscous fluid in the core, bamboo waves. *Phys. Fluids* **13**(4), 841.

https://doi.org/10.1017/S0022112007008269 Published online by Cambridge University Press

Kouris, C. & Tsamopoulos, J. 2002*a* Core–annular flow in a periodically constricted circular tube. Part 2. Nonlinear dynamics. *J. Fluid Mech.* **470**, 181.

Kouris, C. & Tsamopoulos, J. 2002*b* Dynamics of axisymmetric core–annular flow in a straight tube. ii. The less viscous fluid in the core, saw tooth waves. *Phys. Fluids* **14**(3), 1011.

Kuang, J., Maxworthy, T. & Petitjeans, P. 2003 Miscible displacements between silicone oils in capillary tubes. *Eur. J. Mech.* **22**, 271.

Li, J. & Renardy, Y. Y. 1999 Direct simulation of unsteady axisymmetric core–annular flow with high viscosity ratio. *J. Fluid Mech.* **391**, 123.

Loewenherz, D. S. & Lawrence, C. J. 1989 The effect of viscosity stratification on the instability of a free surface flow at low Reynolds number. *Phys. Fluids* A **1**, 1686.

Mack, I. M. 1976 A numerical study of the temporal eigenvalue spectrum of Blasius boundary layer flow. *J. Fluid Mech.* **73**, 497.

Malik, S. V. & Hooper, A. P. 2005 Linear stability and energy growth of viscosity stratified flows. *Phys. Fluids* **17**, 024101.

Panton, R. L. 1984 *Incompressible Flow*. John Wiley.

Petitjeans, P. & Maxworthy, T. 1996 Miscible displacements in capillary tubes. Part 1. Experiments. *J. Fluid Mech.* **326**, 37.

Preziosi, L., Chen, K. & Joseph, D. D. 1989 Lubricated pipelining: stability of core–annular flow. *J. Fluid Mech.* **201**, 323.

Ranganathan, B. T. & Govindarajan, R. 2001 Stabilization and destabilization of channel flow by the location of viscosity-stratified fluid layer. *Phys. Fluids* **13**(1), 1–3.

Riaz, A., Pankiewitz, C. & Meiburg, E. 2004 Linear stability of radial displacements in porous media: influence of velocity-induced dispersion and concentration-dependent diffusion. *Phys. Fluids* **16**(10), 3592.

Sahu, K. C. & Govindarajan, R. 2005 Stability of flow through a slowly diverging pipe. *J. Fluid Mech.* **531**, 325.

Schmid, P. J. & Henningson, D. S. 2001 *Stability and Transition in Shear Flows*. Springer.

Scoffoni, J., Lajeunesse, E. & Homsy, G. M. 2001 Interface instabilities during displacements of two miscible fluids in a vertical pipe. *Phys. Fluids* **13**(3), 553.

Smith, M. K. 1990 The mechanism for the long-wave instability in thin liquid films. *J. Fluid Mech.* **217**, 469.

Tan, C. T. & Homsy, G. M. 1986 Stability of miscible displacements: rectilinear flow. *Phys. Fluids* **29**, 73549.

Taylor, G. I. 1960 Deposition of a viscous fluid on the wall of a tube. *J. Fluid Mech.* **10**, 161.

Vanaparthy, S. H., Barthe, C. & Meiburg, E. 2006 Density-driven instabilities in capillary tubes: influence of a variable diffusion coefficient. *Phys. Fluids* **18**, 048101.

Wei, H. H. & Rumschitzki, D. S. 2002*a* The linear stability of a core–annular flow in an asymptotically corrugated tube. *J. Fluid Mech.* **466**, 113.

Wei, H. H. & Rumschitzki, D. S. 2002*b* The weakly nonlinear interfacial stability of a core–annular flow in a corrugated tube. *J. Fluid Mech.* **466**, 149.

Yih, C.-S. 1967 Instability due to viscous stratification. *J. Fluid Mech.* **27**, 337.

https://doi.org/10.1017/S0022112007008269 Published online by Cambridge University Press